Sesame-cookie topography silver nanoparticles modified carbon nanotube paper for enhancing lightning strike protection

Hetao Chu [a], Qianshan Xia [a], Zhichun Zhang [a], Yanju Liu [b], Jinsong Leng [a, *]

[a] Center for Composite Materials and Structures, No. 2 YiKuang Street, Science Park of Harbin Institute of Technology (HIT), Harbin, 150080, PR China
[b] Department of Aerospace Science and Mechanics, No. 92 West DaZhi Street, Harbin Institute of Technology (HIT), Harbin, 150001, PR China

ABSTRACT

Aircrafts are increasingly fabricated by carbon fiber reinforced polymer (CFRP) composites, because of the excellent specific stiffness and strength. However, lower electrical conductivity, leads to the drawback of the aircraft to lightning strike protection (LSP) changing from conductive metals to insulate composites. Herein, a sesame-cookie topography silver nanoparticle modified carbon nanotube paper (SMCNP) protective layer was developed to enhance LSP efficiency on the CFRP. The integrated material, SMCNP, could be molded directly on the surface layout of CFRP without any insulating adhesives. By contrast, carbon nanotube paper (CNP) and SMCNP were systematically studied on the influence of LSP and the possible protection mechanisms were discussed. Sesame-cookie silver nanoparticle not only enhances the electric conductivity, from 323 S/cm to 3600 S/cm in 14.14 wt%, but also provides a melted silver skeleton for extending current conduction along protection layer illustrated from the XPS and Raman analysis. SMCNP-CFRP maintains 92.1% residual mechanical property after simulated LS interaction which is much higher than that unprotected CFRP of 65.9%.

© 2018 Elsevier Ltd. All rights reserved.

1. Introduction

CFRP composites have been extensively applied in aircraft wind turbine blade components for a variety of applications where the lightweight, high strength [1] and corrosion resistance are primary concerns, because of their specific strength and stiffness. Boeing 787 features over 50% CFRP composites [2]. Moreover, CFRP instead of metallic components, leads to fuel efficiency increased, maintenance expense reduced and fatigue and corrosion resistance characteristics increased. Lightning strike (LS) is a kind of natural disaster threatens all aircraft and wind turbine blade structures [3—5], whether metal or their composites by melting at lightning attached points [4], Joule heat [5], electromagnetic interference [6], and igniting vapors of the fuel tank [6,7]. All the airplanes will be undergone lightning strike more than once a year on average [8,9], thus LSP is an important consideration taken into account in designing new aircraft [9]. The metallic LSP structures [10], such as the traditional aluminum airframes are electrically conductive enough to dissipate the LS energy [10,11]. Although carbon fiber (CF) is a better conductor, the polymer as an insulating matrix decreases the overall conductivity of CFRP. Therefore, CFRP composite structures are usually inferior electrical and thermal conductivity as metallic materials which are hardly survived suffered a LS with the current around 40-100 KA generating catastrophic failure of aircraft systems such as fuel tanks and electronic systems [12]. To overcome this shortcoming of low conductivity in lightweight CFRP, incorporating of metal meshes [13], metal foils [12—15], carbon nanofibers [6,15—18], and various composites are being studied [17—21]. However, applying metallic lightning protection system increases the total structural weight, reducing the fuel saving, as well as the manufacturing complexity [2]. In addition, regarding the electrical properties, in spite of metallic protection system possess high electrical conductivity to withstand lightning current and permeability affect the metallic features result in the tendency of corrosion and degradation in long-term application [1,2,22]. For commercial metallic protection system, wove mesh used on Boeing 787 for LS protection is manufactured using strands of alloyed metal [15], which causes roughness of airplane surface at cross points due to localized double wire thickness. Increased roughness caused by screening mesh over outer structure requires more resin volume to fill the metallic mesh to provide a smooth surface, leading to increasing the total weight of the structure. For some special requirements, metal meshes need

isolation layer and bonding medium [2], such as adhesives, resins, or surface films, to attach to composite substrate via piling separate layer, prepreg, or a ply integrated solution. Typically, metal mesh is placed between two sandwich adhesive films [2,19]. For separate plies case, metallic mesh is embedded into uppermost layer of CFRP structure and surface adhesive is required to protect metal mesh from outside elements, such as air and water vapor [2,19]. Although metallic mesh is protected by surface adhesive, the water vapor absorption and cool-warm cycling (−60−40 °C) will lead slow corrosion of mesh and aging of polymer affect adhesive force between interfaces. Owing to poor resin compatibility of metal, metallic mesh will break away from CFRP structure in a long time [23−26]. These complicated manufactory process inevitably decrease productive efficiency for practical application.

To combat the drawbacks of metallic mesh in LS protection system, several studies have paid much attention to lightweight conductive fillers [27,28], such as carbon nanotubes [29,30], carbon nanofibers [6,28], and graphene [30], as the alternatives to the traditional metallic lightning protection materials. Divya et al. [19] investigated the effect of nickel particle modified single walled carbon nanotubes filled in carbon fiber-bismaleimide composite for LS protection. They observe that the modified nanofillers able to enhance carbon nanotube dispersion and provide uniform surface coverage on the carbon plies. Gou et al. [6] showed a positive correlation between conductivity of carbon nanofiber paper and improvement of LS protection. Zhang et al. [29] systematically studied galvanic corrosion effects of Al/Cu meshes with graphene, carbon fiber and ITO nanocomposites as a new approach for LS protection. Jinhua et al. [30] investigated the effect of various insulation layers for LS protection of manual adhered carbon nanotube paper/carbon fiber composite. For the above reports, on the one hand, conductive nanofillers and coatings are still hard to maintain high dispersion in various resins, especially an arduous work for prepreg manufacturing. Typically, the existing carbon fiber composite materials are prepared by precursor of prepreg, while nanofillers are difficult to integrate carbon fiber forming prepreg. On the other hand, the reported carbon nanofiber paper, buckypaper, or graphene paper required specific insulating layer [2,30] to increase the LS protection performance resulting in complicated fabricated process in practical application. Moreover, the manual adhered protection layer inevitably decreases production efficiency, due to most CFRP structures are manufactured by the approaches Resin Transfer Molding or vacuum hot-pressing. Therefore, secondary operation is undesired for industrial production.

Carbon nanotube paper (CNP) is a non-woven film structured by CNTs and can be prepared by vacuum filtration method [31,32], floating catalyst growth [33], or draw from carbon nanotube forest [33,34]. Since CNP is derived from CNTs, all the superior properties, such as high electrical conductivity [35], low density [36], high surface area, outstanding corrosion resistance, and excellent mechanical feature, displayed on CNT are all maintained. For the past few years, the applications of CNP have expanded, such as mechanical sensor [22,37,38], deicing [39], electrochemical electrode [39,40], infrared stealth [41], and electromagnetic shielding [42]. Typically, the density of most CNP is less than 0.8 g/cm^3, which is much lower than Cu (8.9 g/cm^3) and Al (2.7 g/cm^3). Moreover, CNP has a better interface compatibility than metallic mesh when it is integrated with various resins, due to the hydrophobic feature of CNT. Therefore, CNP is a promising alternative, lightweight, superior conductivity, for LS protection of carbon fiber composite to overcome the shortcomings generated by metallic mesh materials. In this study, a modified CNP was fabricated by small amount silver nanoparticles via a facile approach with high performance of LS protection. According to

Kirchhoff's law [43], for a conductor, the loading current component is a few of outmost atomic layer for the pathway of electrons. Therefore, small amount of modified silver nanoparticles is able to increase conductivity sharply [44,45]. In addition, the facile modified strategy could maintain the initial resin compatibility. Most important of all, for the presented modified CNP enable directly integrated with carbon fiber prepreg by vacuum hot-pressing without the requirement of insulating layer and surface protection adhesives as the previous reports [2,28]. Non-secondary processing is desired for practical application to increase productive efficiency inevitably.

2. Experimental

2.1. Materials

Pristine SWCNT material, average tube diameter 3−5 nm, length 5−30 nm, were provided from Chengdu Organic Chemicals Co. Ltd., and carbon content was more than 90%. As a surfactant, Triton X-100, biological grade, was obtained from Aladdin Chemical Reagents Co., Ltd.. Silver nitrate was also acquired from Aldrich. Carbon fiber prepreg was provided by Shanghai Kangzhan Composites Co., Ltd., China.

2.2. Measurements

An atomic force microscope (AFM, Bruker Multimode 8) was used to observe the porous structure of CNP using the ScanAsyst in air mode. Scanning electron microscopy (SEM) observations were performed by Quanta 200F Field Emission Scanning Electron Microscope (30 kV). Surface profilometry analysis using a laser confocal microscope (Olympus, OLS3000) to investigate 3D surface structure and roughness. Conductivity was characterized by a Napsom Resistivity Measurement System (RG-7). Thermostability analysis in air atmosphere was measured via Mettler Toledo TGA/DSC1, at a heating rate of 10 °C/min and ranged from room temperature to 1000 °C. Raman spectra were characterized by an Almega-Dispersive (Thermo Nicolet). The executed wavelength is 532 nm with the wave number ranging from 400 to 4000. A micrometrics ASAP 2020 volumetric adsorption analyzer characterized porous structure of CNP at 77 K. Surfaced area was calculated using Barrett-Emmett-Teller (BET) model. X-ray photoelectron spectroscopy (XPS) was executed using a PHI 5700 ESCA System with the Retarding mode of Al Kα X-ray source (1486.6 eV). Mechanical properties were researched by a Zwick/roll Material Testing Machine. Crosshead speed was 2 mm/min, and 5 samples were tested for each valid data. Infrared camera (FLIR) was used to observe the temperature field changing of the LS moment.

2.3. Methods

2.3.1. Preparation of pristine CNP
As our previous report [39], the thickness and areal density of the as-prepared CNP was ~60 μm and 4 mg/cm^2, respectively. To increase the electric conductivity, the CNP was heated at 380 °C in a vacuum oven to remove the residual surfactant.

2.3.2. Fabrication of silver modified CNP (SMCNP)
In order to further increase the electric conductivity, according to the Kirchhoff's law, a small amount silver particle was deposited on one side of CNP via spray-photolytic method, because of keeping the interface compatibility of resin on the other side. Silver nitrate aqueous solution with 0.1 mol/L, was dissolved in deionized water in dark space, was used in the sprayed process. Due to the feature of large surface area, silver and nitrate ions absorb on CNP surface

inevitably. The wet CNPs were dried at 50 °C, and then the adsorption surface of the CNP was exposure under light. It was well known that, typically, silver nitrate decomposed into silver, NO_2 and O_2 under the irradiation of a fluorescent lamp shown in Equation (1) to result silver particles.

$$2AgNo_3 \xrightarrow{light} 2Ag + 2No_2 \uparrow + O_2 \uparrow \tag{1}$$
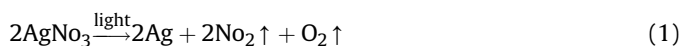
2.3.3. Fabrication of carbon fiber reinforced polymer/SMCNP (SMCNP -CFRP)

SMCNP-CFRP was manufactured by vacuumed hot pressing. The size of CFRP laminate is $300 \times 300 \times 3.2$ mm^3 and each carbon fiber layer was lain with orthogonal ply. Then, the SMCNP was covered onto the outmost layer of the CFRP prepreg. Subsequently, the GFRP-SMCNP composite was integrally vacuumed in a chamber pressure of 0.4 MPa. Fig. S1 displayed the prepared schematic diagram and the layout of the SMCNP-CFRP composite in an integral hot pressing process.

2.3.4. Simulated LS test

The as-prepared GRRP-CNP or GFRP-SMCNP composite panels were subjected to a Zone 2A (subsequent swept strokes) direct effects using a peak current of 100 KA and grouped D, B, and C current waveforms based on the SAE ARP 5412. Component D current waveform represented a subsequent stroke, and component B and C represented the lightning environment that might be caused by the intermediate and long duration currents following the swept strokes. During the test, the composite panels were placed with CNP/SMCNP layer facing the lightning discharge electrode. Electrical charge (Q) and action integral (AI), which indicates the total energy and specific energy of the simulated process, could be expressed as following Equations (2) and (3) where i is the time varying electrical current of lightning waveforms.

$$Q = \int i \mathrm{dt} \tag{2}$$

$$AI = \int i^2 \mathrm{dt} \tag{3}$$

3. Results and discussion

3.1. Morphology characterization of self-assembly CNP and SMCNP

Topography of the large scale self-assembly CNP, after heat treatment, is shown in Fig. 2A with a size of $370 \times 370 \times 0.06$ mm^3. The moderate wrinkles indicate the as-prepared CNP possesses sufficient thin and flexibility. As shown in the inset, a small piece of the as-prepared CNP could be folded a CNP plane easily without any cracks or damage. As for as we known, the superior flexibility is much better than the previous reports [30,46] using the filtered strategy and reaches the same flexible level as well as floating catalyst growth method. In our standpoints, two reasons are in favor of increasing the flexibility. One is the purity of CNTs; the other one is the dispersibility of CNT suspension, because the both aspects could increase physical cross link points between CNT bundles or individual CNT. The shearing dispersion process used in this article enhances the mechanical coating of the surfactant with CNT bundles. Surfactant microemulsion surrounds CNTs in the suspension, When the surfactant concentration over the Critical Micelle Concentration. In that case, the surfactant microemulsion attaches individual CNT

bundles penetrate the porous membrane. Therefore, shear dispersion and surfactant could increase the CNT dispersibility and CNT physical cross points. Owe to the microemulsion in suspension, CNT bundles could deposit step by step packaged in the microemulsion. The amount of physical cross points displays high flexibility and porosity of the as-prepared CNP. Superior flexibility is a key factor for the manufacturing in the practical application, especially for integral hot pressing process. Fig. 1B presented porosity of the pristine CNP that underwent heat treatment. It is clear the CNT bundles are entangled with each other forming a porous CNT network. Due to the high dispersibility and the template of microemulsion, a large number of physical crosslinking points are achieved depending on the electrostatic force. However, the as-prepared CNP before heat treatment (Fig. S2) presents many amorphous particles distributed in the holes of network or attach on CNT bundles which is caused by the aggregation of residual surfactant. Due to the decomposition of surfactant by heat treatment, the porosity of the as-prepared CNP is achieved to produce an isotropous non-woven CNT paper. Fig. 1C shows cross section image of the porous CNP prepared by FIB with the gallium plasma. The front surface of the square hole is the cross section face. Due to the self-assembly sedimentation and overlap joint process, CNT bundles develop many interspaces and porous structures inside of CNP. The enlarged photograph of cross section face is shown in the inset of Fig. 1C indicating a porous topographical feature of the inner CNP. On the one hand, porosity topography is in favor of resin penetration when the CNP was integrally processed with CFRP by hot pressing with the detail comparison in the later discussion. On the other hand, the porous structure provides the attachment points for silver nanoparticles. The pores increase surface area of the CNP and higher silver particle loading capacity is produced without leading to blind off the pores, which means the resin penetrating feature is maintained in the subsequent processing. Good permeability is a significant property when the panels are attacked by LS. As-prepared CNP after silver nanoparticle modified is presented in Fig. 1D. The silver nanoparticles were obtained after the photolysis under a fluorescent lamp. As presented in the photograph, uniform size silver nanoparticles attach on CNT bundles discretely with the diameter ~25 nm. It is apparent silver nanoparticles also fill in the holes constructed by CNT bundles meaning the high adsorbability of the silver nanoparticles on CNT networks. The embedded silver nanoparticles form sesame-cookies SMCNP that silver nanoparticles as the sesame are fixed in cookies part of porous CNP frame which is further explained in the later part. In addition, the porous feature is still maintained leading to the channel for resin penetration in hot pressing process. The silver particle size distribution and pore structure are demonstrated in Fig. 1E. Obviously, the tendency of diameter distribution complies with Gaussian distribution mainly locating in the range of 20−30 nm. The good uniformity indicates the photolysis strategy is useful for obtaining nanoparticle modified CNP extensively and rapidly. Porous feature of CNP and SMCNP was displayed in Fig. S3. CNP and SMCNP basically follow the type IV isotherm with H1 hysteresis loop (Fig. S3A). The uniform pore structure and H1 hysteresis is the evidence that CNP and SMCNP are mesoporous materials. Pore diameter distribution is shown in Fig. S3B. The peaks of CNP and SMCNP are located at ~12−18 nm. Therefore, the sprayed photolysis is a more facile strategy compared with the electrochemical method for depositing silver nanoparticles on CNP substrate on a large scale, which is an important condition for engineering application. The compared cross section photograph of the CNP and SMCNP is displayed in Fig. S4. In Fig. S4A, cross section of the neat CNP is consisted by random CNT networks. It is obvious that the neat CNP is a flexible sheet with the thickness about 30 μm. Fig. S4B shows the topography of SMCNP. As can be seen in picture, a large amount of silver particles are embedded in the frame of CNP just like the structure of sesame in cookie (white dots). The
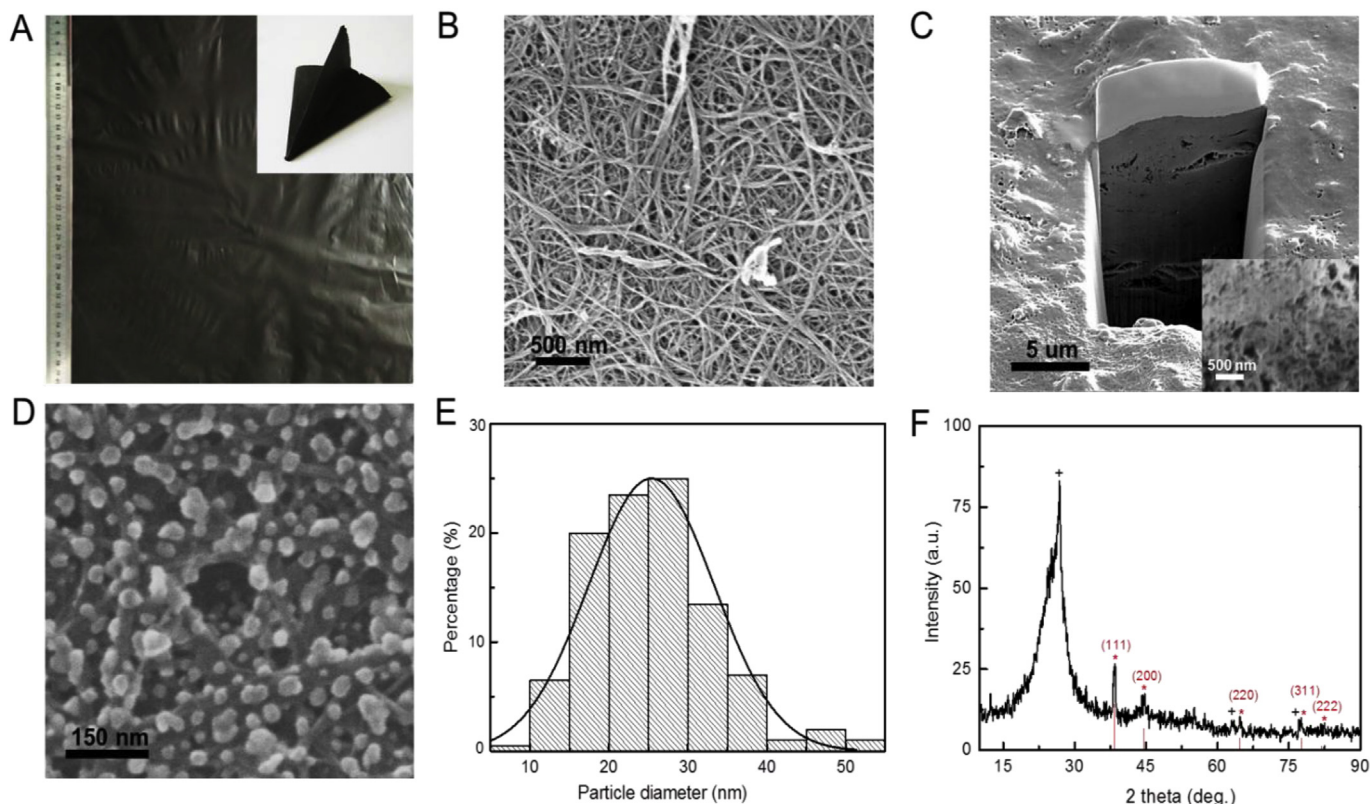
Fig. 1. (A) The digital image of the as-prepared CNP after heating treatment. Inset is a CNP plane showing high flexibility. (B) High magnification SEM of the CNP after heating treatment. (C) Cross section photograph of Fig. 1B fabricated by FIB strategy. Insert picture is enlarged part of the cross section surface. (D) SEM image of the SMCNP after photolysis. (E) Size distribution and Gaussian distribution curve of the silver particles of Fig. 1D. (F) XRD pattern of the SMCNP. Crossing signs indicate the peaks of CNP while star signs show the peaks of silver particles. (A colour version of this figure can be viewed online.)

inset is the zoom in photograph illustrating a clear sesame-cookie structure. The white dots indicate silver particles distribute in the CNP frame uniformly. Based on Fig. 1D and S3B, modified silver nanoparticles are embedded in the entire of CNP forming a sesame-cookie structure. XRD patterns of the SMCNP composite is shown in Fig. 1F with the sprayed face toward the detector of XRD. Typically, three characteristic diffraction peaks at 26.6°, 63.7°, and 77.7° (plus signs) attributed to (003), (015), and (110) reflections of graphitic carbon respectively (PDF#26-1079). In addition, silver nanoparticles show five significant diffraction peaks, which coincides with the (111), (200), (220), (311) and (222) planes (star signs) in the standard Ag spectrum (PDF#65-2871). Raman spectra of SMCNP, CNP and the pristine CNTs are demonstrated in Fig. S5. The value of I_D/I_G is 0.044, 0.036, and 0.022, respectively. The tiny change manifests the processes of shearing and ultrasonic dispersion, and particle modification causes weak defects of CNT.

3.2. Morphology analysis of CNP-CFRP/SMCNP-CFRP

LS protection panels were prepared by vacuum hot-pressing. Three types samples, neat CFRP panel, CNP-CFRP panel, and SMCNP-CFRP panel, are displayed in Fig. 2A, B, and C. As illustrated in Fig. 2(A-C), smooth surface is obtained in all samples, due to resin penetration. The smooth surface demonstrates the pore structure of CNP and SMCNP is useful for resin penetration during the hot-pressing. In addition, the smooth surface indicates the sesame-cookies maintain the channel for resin penetration. In this case, the CNP/SMCNP layer can attach closely on the CFRP matrix under the ultra-high pressure impact of a LS, which is a significant factor

for LS protection. Fig. 2(D-F) are the cross section images of three kinds of samples. The neat CFRP matrix clearly shows the orthogonal layout of carbon fiber ply with epoxy resin filling in the space between carbon fiber filaments. CNP-CFRP and SMCNP-CFRP composite cross section pictures (Fig. 2E and F) express the protective layers of CNP and SMCNP adhere compactly on the outside of CFRP matrix surface meaning a good resin permeability and compatibility. Compared with the CNP layer, the SMCNP layer is much rougher with many silver particles embedded inside of CNP frame. The thickness of a protective layer is about 60 μm the same with as-prepared paper thickness.

Fig. 2(G-I) are the SEM images of the corresponding panel surface. Black regions indicate the surface epoxy of neat CFRP panel and infiltrated epoxy of CNP-CFRP and SMCNP-CFRP panels. The pictures reveal that epoxy resin could well penetrate the CNP and SMCNP to fix protecting layers on the matrix surface. For the SMCNP-CFRP composite, the silver nanoparticles embedded in CNP frame could be melted and confirm the CNT bundle to undertake Joule heat and current at the high temperature and air pressure at the attacking moment of LS. Surface roughness corresponding to Fig. 2(A-C) is measured by confocal microscope shown in Fig. S6. Fig. S6 (A-C) are the 2-D images of neat panel, CNP-CFRP panel and SMCNP-CFRP panel. Red lines (Fig. S6A) and red dots (Fig. S6C) indicate the aligned carbon fiber and silver particles. Green and blue colors on the surface manifest the infiltrated epoxy resin of CNP and SMCNP. Surface roughness is calculated from 3-D images shown in Fig. S6(D-F). The value of average surface roughness (SRa) of neat panel, CNP-CFRP panel and SMCNP-CFRP panel are 0.13, 0.09 and 0.11 μm, respectively.
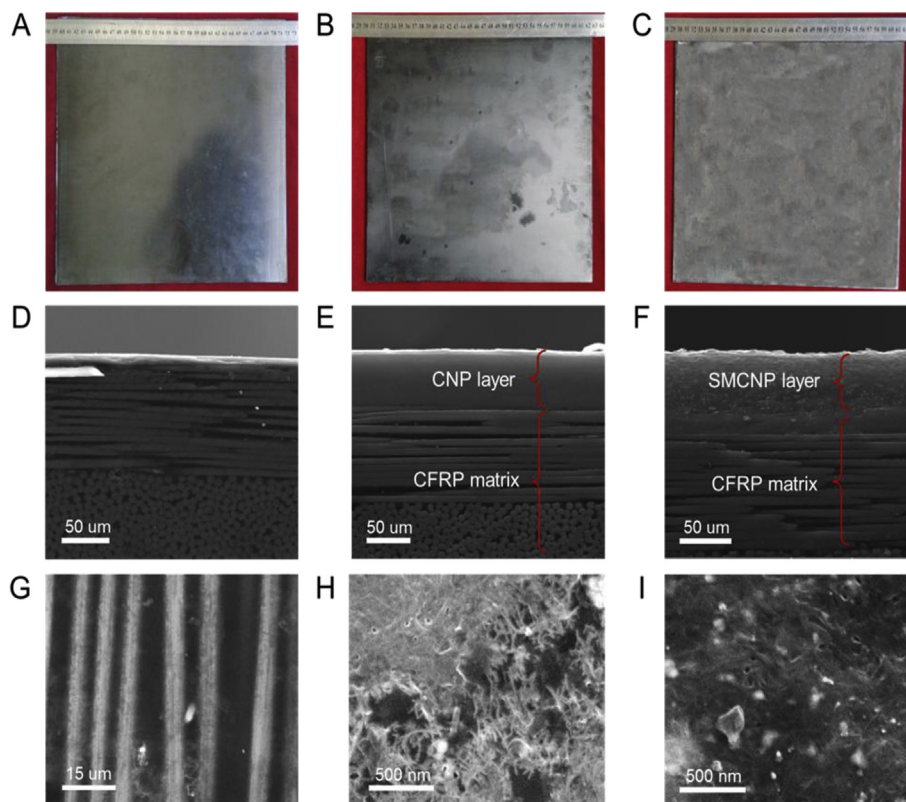
Fig. 2. Digital pictures of the panels are shown in Fig. 2(A—C): (A) neat CFRP panel, (B) CNP-CFRP panel, and (C) SMCNP-CFRP panel. Cross section morphologies of different types of composite panels in Fig. 2(D—F): (D) neat CFRP panel, (E) CNP-CFRP panel, and (F) SMCNP-CFRP panel. Microstructures of the different panels are observed in Fig. 2(G—I): (G) neat CFRP panel, aligned carbon fiber and resin regions arranged alternatively, (H) CNP-CFRP panel, and (I) SMCNP-CFRP panel. (A colour version of this figure can be viewed online.)

3.3. Conductivity performance analysis

The conductivity of the SMCNP sprayed by different concentration silver nitrate solution is shown in Fig. 3A. Column bar indicates the conductivity of as-prepared CNP after the heat treatment with the value of 323 S/cm. The black curve reveals the as-prepared CNP after spraying process by different concentration of silver nitrate. It is apparent that, after spraying, the conductivity has moderate enhancement from ~300 S/cm to ~600 S/cm, due to tiny photolysis of the silver nitride. Nevertheless, the conductivities

increase dramatically after photolysis exposed in fluorescent lamp. As increased of sprayed concentration, the conductivity increases rapidly first, while in the high sprayed concentration, the conductivity increases slowly fluctuating at a constant value about ~3600 S/cm. The sharp increase is generated by the part of silver nanoparticles synthesized from photolysis reaction. For the constant part curve, the reason is produced by equilibrium of the adsorbing capacity of CNP porosity. The adsorbing quality could not be increased when the porous structure reaches to the maximum capacity. In this paper, 2.0 mol/L was operated for preparing the
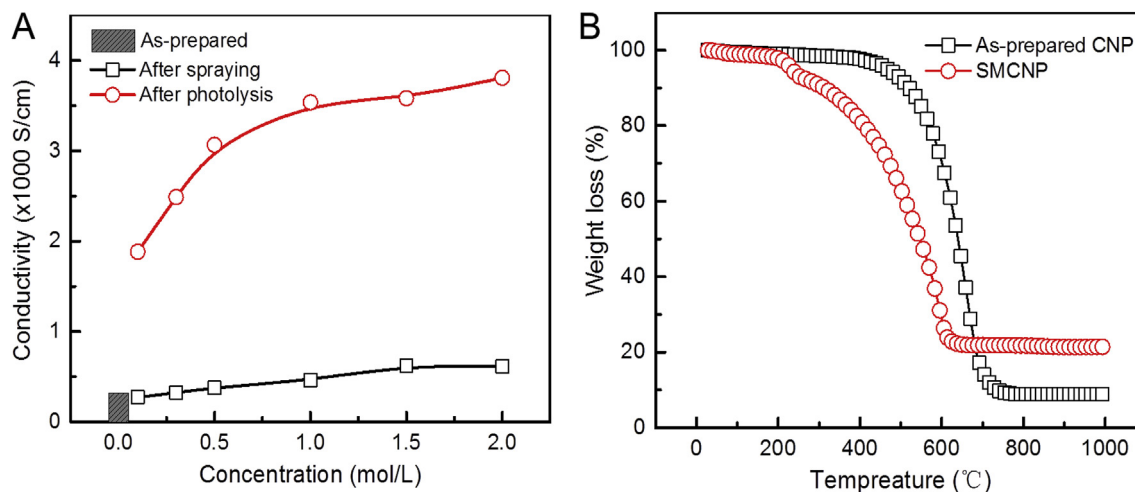
Fig. 3. (A) Conductivity of the as-prepared samples and sprayed samples before and after photolysis. (B) TGA curves of as-prepared CNP and sprayed SMCNP by 2.0 mol/L silver nitride solutions. (A colour version of this figure can be viewed online.)

SMCNP-CFRP panels.

To investigate the corresponding mass of silver nanoparticles of SMCNP, TGA was implemented to calculate the mass of silver nanoparticles of the SMCNP deposited by 2.0 mol/L silver nitride. Fig. 3B conducts the TGA curves of CNP and SMCNP carried out in air atmosphere. Apparently, the as-prepared CNP decomposes dramatically at 650 °C and terminates at 800 °C. Terminal mass, 8.8%, represents the residual catalyst in the raw material of CNT. For the SMCNP, the residual mass is 21.7% including silver nanoparticles and catalyst. Owe to the same percentage of catalyst in both CNP and SMCNP, the mass of silver nanoparticles is approximately 14.14% with the atomic ratio of 54.6:1 (C: Ag).

3.4. Simulated LS test and analysis

Simulated LS test was executed by capacitor discharge procedure subjected to a Zone 2A. The generator is capable of producing artificial lightning wave of D, B and C according to the SAE ARP 5412 with the discharge moment displayed in Fig. S7. Electrical Charge (Q) and action integral (AI) demonstrated Equations (2) and (3) are presented in Fig. 4. Fig. 4(A-C) are the current waveforms induced by capacitive impulse. Component D (Fig. 4A) represents a restrike current and generates a more than 10 atmospheric pressure on CFRP composite. Thus, the failure mode of component D is the impulse damage. The oscillatory waveform displays peak amplitude of 100 KA and an action integral. Component B (Fig. 4B) is the

intermediate current with an average amplitude of 2 kA flowing for a maximum duration of 5 ms. However, component C (Fig. 4C) stands for the continuing current. Component B and C generate a huge Joule heat and make the surface temperature of CFRP composite is over 3000 °C. Thus, the failure mode of component B and C is the heat and ablation damage. The action integral, peak current, average current and electrical charge is listed in Fig. 4D, respectively [47—50].

The digital images of the neat panel, CNP-CFRP panel, and SMCNP-CFRP panel after simulated LS are presents in Fig. 5(A-C). In Fig. 5A, significant severe damage is generated and a few layers of carbon fiber are cracked under the high energy impact forming fiber damaged area of 151 × 126 mm^2 in the blue circle detected by C scope image of Fig. 5D. However, the fiber damaged area is decreased dramatically after integrating the protection CNP layer with the fiber damaged area of 30 × 50 mm^2 in the blue circle of Fig. 5B and E, while the CNP damaged area is about 199 × 173 mm^2 in the red circle indicating CNP is a sacrificial layer for dispersing energy to protect carbon fiber matrix. From the ablation edge topography, CNP layer experienced high temperature erosion and high air pressure impact during simulated LS. Fig. 5C is the SMCNP-CFRP panel after LS showing only the top few layers of carbon fiber are broken by the LS with fiber damaged area of 55 × 50 mm^2 in the blue circle represented in Fig. 5F. Moreover, from the Fig. 5 F, SMCNP-CFRP damaged area is about 189 × 177 mm^2 marked in the red circle. Compared Fig. 5B with Fig. 5C, fiber damaged area of

	D wave	B wave	C wave
$I_{peak/avg}$ (kA)	100	2	0.4
AI(A^{2}s)	0.25 x 10^6	——	——
Q(C)	——	10	21
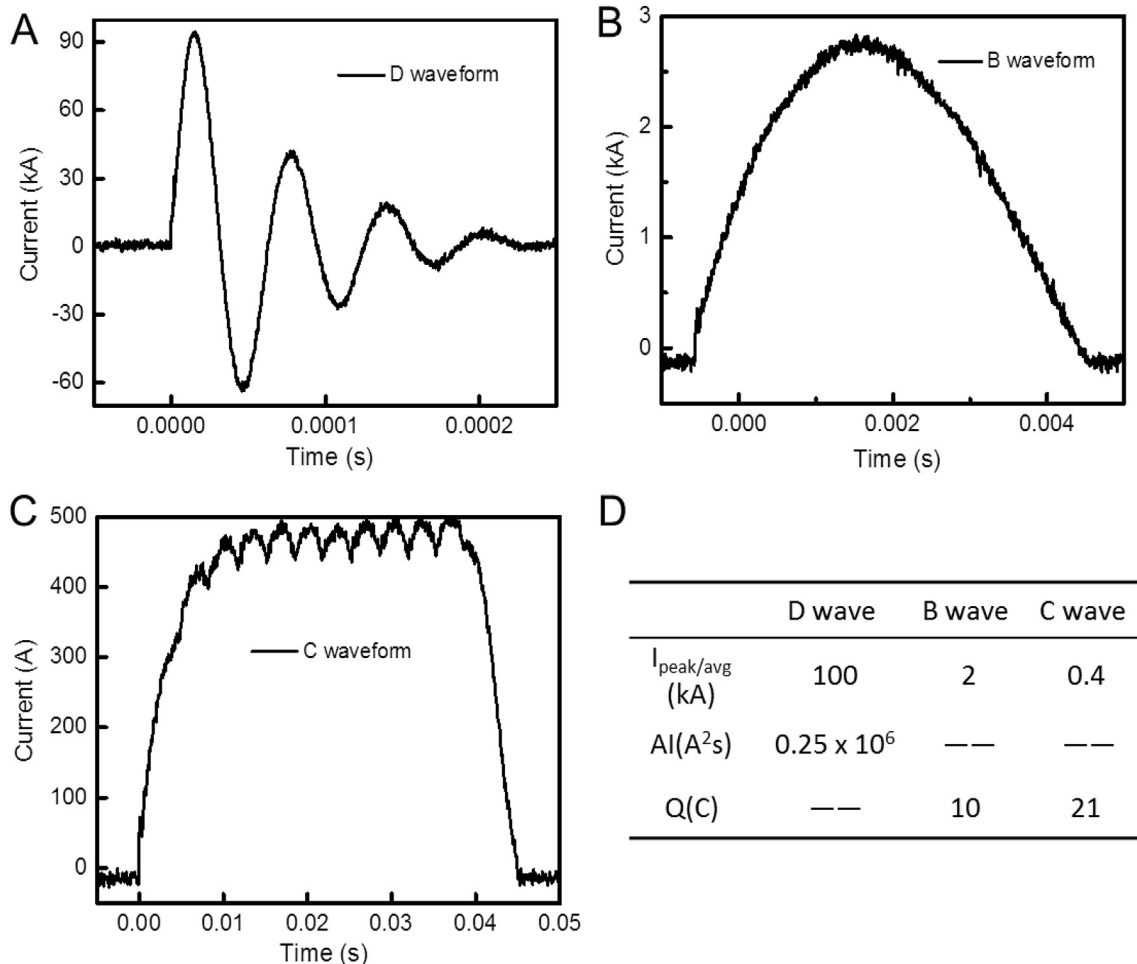
Fig. 4. (A) Component D waveform of the simulated LS. (B) Component B waveform. (C) Component C waveform. (D) Parameters of the waveforms.
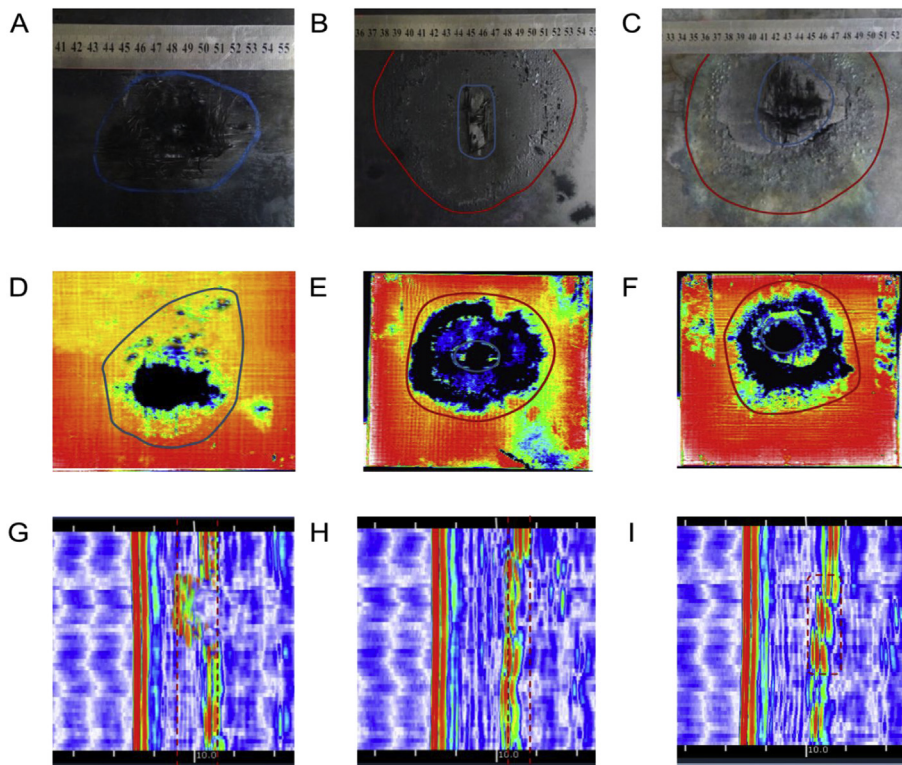
Fig. 5. The digital images of the laminates after simulated lighting strike: (A) neat CFRP panel, (B) CNP-CFRP panel, and(C) SMCNP-CFRP panel; Non-destructive inspection of the samples after LS tests: (D) typical C scope image of neat CFRP panel, (E) C scope image of CNP-CFRP panel, and (F) C scope image of SMCNP-CFRP panel, (G) typical B scope image of neat CFRP panel, (E) B scope image of CNP-CFRP panel, and (F) B scope image of SMCNP-CFRP panel. (A colour version of this figure can be viewed online.)

CNP-CFRP is smaller than SMCNP-CFRP. In addition, broken fiber edge of CNP-CFRP is dehiscent while the SMCNP-CFRP is capillaceous, which illustrates different protective mechanism, discussed in the later analysis, for CNP-CFRP and SMCNP-CFRP in the two cases. Moreover, the ablation edge of SMCNP is a tough and brittle rupture indicating SMCNP is a harder protective layer than CNP. Fig. 5(G-I) are the typical B scope image for the corresponding panels. The thickness between two red faces is the viewing angle of laminate cross section. The distance between two red dashed lines shows the depth of damaged carbon fiber. Because of 4 mm thickness of each panel, the depth of neat CFRP panel, CNP-CFRP panel, and SMCNP-CFRP panel is ~2 mm, ~0.8 mm, and ~0.3 mm, respectively. Neat CFRP panel has an obvious damage than CNP-CFRP and SMCNP-CFRP panels. Compared Fig. 5H and I, ~7–8 layers of carbon fiber ply of CNP-CFRP panel are fractured at the utmost depth segment while local fracture is generated of the surface carbon fiber ply of SMCNP-CFRP panel surrounded in the red dashed line rectangular (Fig. 5I). Therefore, for CNP-CFRP panel, carbon fiber damaged area is smaller than SMCNP-CFRP panel but the utmost damaged depth is thicker than SMCNP-CFRP panel presented in Fig. S8 observed by optical microscope. Fig. S8A shows the carbon fiber broken area of CNP-CFRP, which indicates destruction in the thickness direction. However, broken carbon fiber area of SMCNP-CFRP (Fig. S8B) reveals the in plane (carbon fiber ply) destruction with the clear underlying carbon fiber ply. The damaged depth is a harmful parameter for CFRP structure because of affecting mechanical property directly in engineering applications.

3.5. Protective mechanism analysis of CNP and SMCNP

When the lightning strikes on the surface of CFRP panel, the current flows from carbon fibers, and generates huge Joule heat and

over 3000 °C of high temperature. It makes the ablation of epoxy matrix and carbon fibers leads pyrolysis of epoxy and fusing of carbon fiber. As declared in the previous analysis, CNP-CFRP and SMCNP-CFRP have different protection mechanism due to the damaged topography of ablation edge of the protective layer and cracking area of carbon fiber. Fig. 6A is the CNP ablation edge of CNP-CFRP panel. Compared with Fig. 1B, carbon nanotube bundles keep the initial morphology after impact of LS current. In the enlarged image, the carbon nanotube or bundle shapes are in perfect condition after the high energy effect. The lightning strikes on the surface of CNP-CFRP panel, the current flows from CNP and generates huge Joule heat. Part of energy is conducted, and the others impact on CFRP laminate. It generates the explosion inside the CFRP laminate and makes damage of CNP and several surface layers in CFRP laminate. Fig. 6B is the ablation edge of SMCNP-CFRP panel. Due to the Joule heat of the high LS current, silver particles are melted and gathered together. According to the previous report [2], the attachment point temperature of a LS is ~3000 °C–30000 °C and the air pressure at the attachment point is ~10 atm. For SMCNP protection layer, some silver particles was taken away by a surface explosion that was generated from Joule heat and the direct heat from the plasma channel. The other melted silver particles form a rigid skeleton that is able to fix the CNP on panel surface under the giant air pressure. The silver framework could not only maintain the electric conductivity of SMCNP but also resist the SMCNP layer to be blown away by the high air pressure, which provides a longer current conduction time than CNP-CFRP protection strategy. From the high magnification carbon nanotube image, it obvious carbon nanotube bundles are oxidized by the serious ablation. Carbon nanotube is significantly damaged due to the long term of Joule heat of current conduction. The long current conduction time result in more energy dispersion through the
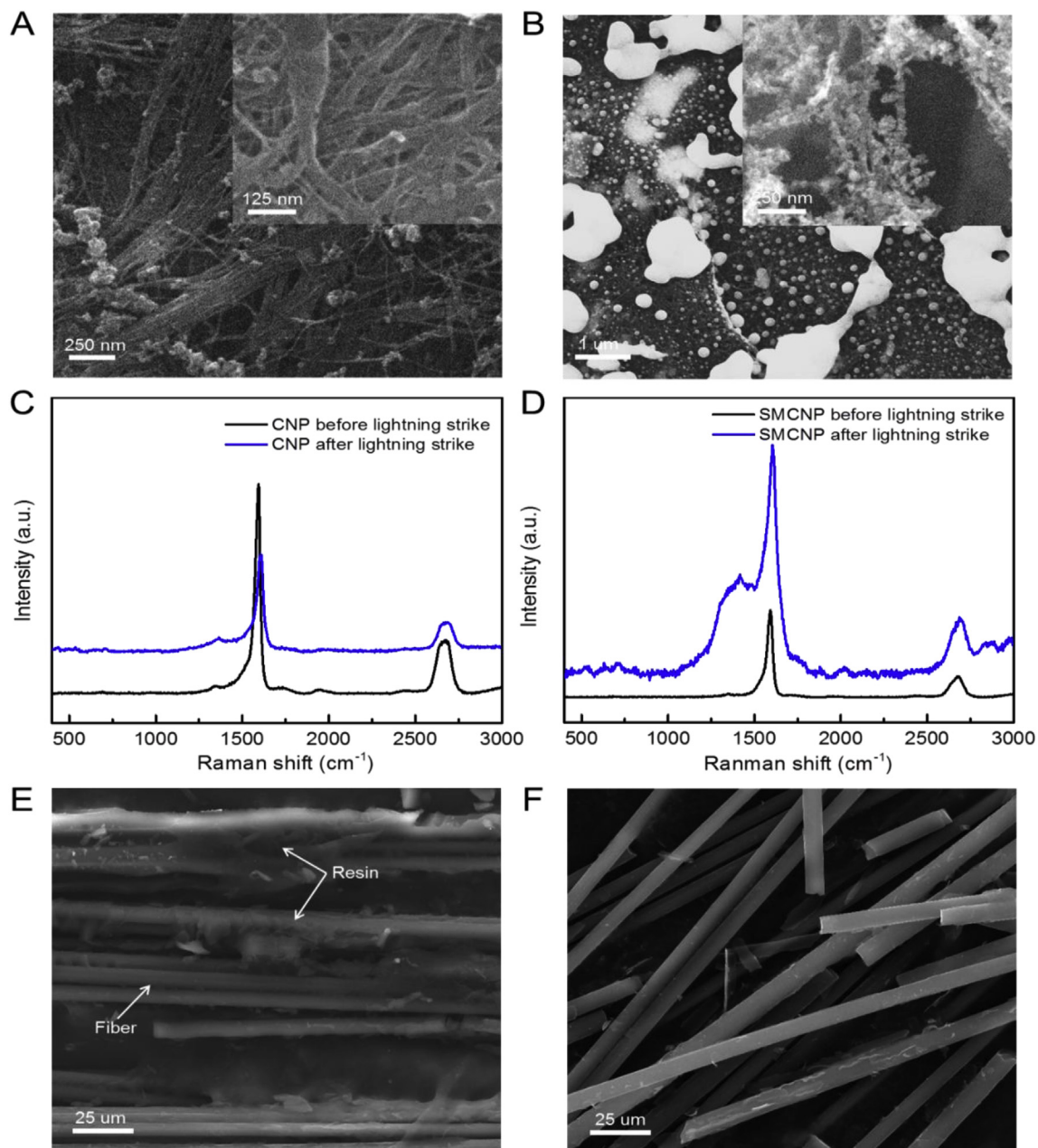
Fig. 6. (A) SEM image of the CNP ablation edge of CNP- CFRP panel. Inset is a partially enlarged image. (B) SEM image of the SMCNP ablation edge of SMCNP-CFRP panel. Inset is a partially enlarged image. (C) Raman spectra of the CNP before and after the LS. (D) Raman spectra of the SMCNP before and after the LS. (E) SEM image of broken carbon fiber of CNP-CFRP panel. (F) SEM image of broken carbon fiber of SMCNP-CFRP panel. (A colour version of this figure can be viewed online.)

protective layer and lead to significantly oxidized of the carbon nanotube.

To investigate the chemical feature of carbon nanotube before and after the LS, carbon nanotube defect is characterized by Raman spectra shown in Fig. 6C and D. As shown in Fig. 6C, intensity of D band indicates the defected feature of carbon nanotube. Typically, the value of I_D/I_G is a significate parameter to evaluate chemical defects on carbon nanotube. The value of CNP, shown in Fig. 6A, before and after the LS is 0.036 and 0.13, respectively. Therefore, after the LS, the intensity of CNP chemical defect increases by ~3 times. Raman spectra of the SMCNP shown in Fig. 6B are presented in Fig. 6D. By comparison, I_D/I_G of the SMCNP before and after the LS is 0.038 and 0.44, respectively, which is increased by ~12 times after the Joule heat ablation.

The chemical defect significant increase is corresponding to the carbon nanotube morphology of Fig. 6B caused by the high temperature oxidization. Therefore, the Raman spectra supports the above discussion that SMCNP-CFRP has a longer current conduction time than CNP-CFRP because silver skeleton attaches carbon nanotube to resist the air pressure impact. In this case, more LS current is conducted in plane of SMCNP layer than CNP layer and less current is conducted out of plane (thickness direction). SEM images of broken carbon fiber of CNP-CFRP and SMCNP-CFRP are demonstrated in Fig. 6E and F. For CNP-CFRP panel (Fig. 6E), it is clear that epoxy resin is still coated on carbon fiber filaments after LS impact as displayed in the bulky segment. Carbon fiber filaments are assembled with the initial epoxy resin, because a small amount of Joule heat is produced on the surface carbon fiber ply. Fig. 6F is

the broken fiber morphology of SMCNP-CFRP panel shown in Fig. 5C. Apparently, epoxy resin of the initial prepreg is decomposed totally after the LS, because of Joule heat of LS current. Moreover, carbon fiber filaments are cracked seriously by the air pressure impact and heat of ablation. Morphologies of Fig. 6E and F well explain the image feature of Fig. 5B and C.

XPS can provide useful information on the nature of functional groups and the presence of structural defects on CNT surface. In Fig. 7(A-D), the XPS survey scan shows the elements of C1s, O1s, Ag3d, and Ag3p (3p$_{3/2}$ and 3p$_{1/2}$) peaks of the CNP and SMCNP before and after the LS is presented. The characteristic peaks are marked in the Figures. Based on the Raman spectra analysis, the feature of carbon nanotube is changed of CNP and SMCNP before and after LS impact, due to oxidation and even combustion reactions at the moment of LS. Therefore, the components of C1s are a useful parameter for discussing the protection mechanism of CNP-CFRP and SMCNP-CFRP. Deconvolution of C1s peak of CNP and SMCNP before and after the LS is illustrated in the bottom of Fig. 7(A-D). The main peak at 284.5 eV is generated from both sp^2-hybridized graphite-like carbon atoms and carbon atoms bound to

Table 1
Atomic concentration of different chemical carbon atoms calculated by XPS.

Atomic concentration	sp^2 C (%)	sp^3 C (%)	C-O (%)	C=O (%)	π-π*(%)
CNP before LS	64.1	8.8	14	6.1	6.9
CNP after LS	66.3	13.1	10.1	2.1	8.4
SMCNP before LS	73.2	7.3	5.6	7.0	7.0
SMCNP after LS	73.2	23.7	3.1	–	–

hydrogen atoms in accord with the previous photoemission studies on CNTs. The peak at 285.1 eV is attributed to sp^3-hybridized carbon atoms as in diamond-like carbon (defect on the carbon nanotube structure). The peaks with higher binding energy located at 286.1 eV and 287.5 eV are assigned to carbon atoms bound to one or two oxygen atoms respectively, because electronegative oxygen atom provides a positive charge on a carbon atom. Therefore, carbon atoms originate in carbon single bond to oxygen in phenol and ether (C-O) and carbon double bond to oxygen in ketone and quinones (C=O). Moreover, binding energy located at 291.5 eV is the characteristic shakeup line of carbon in aromatic compounds. The
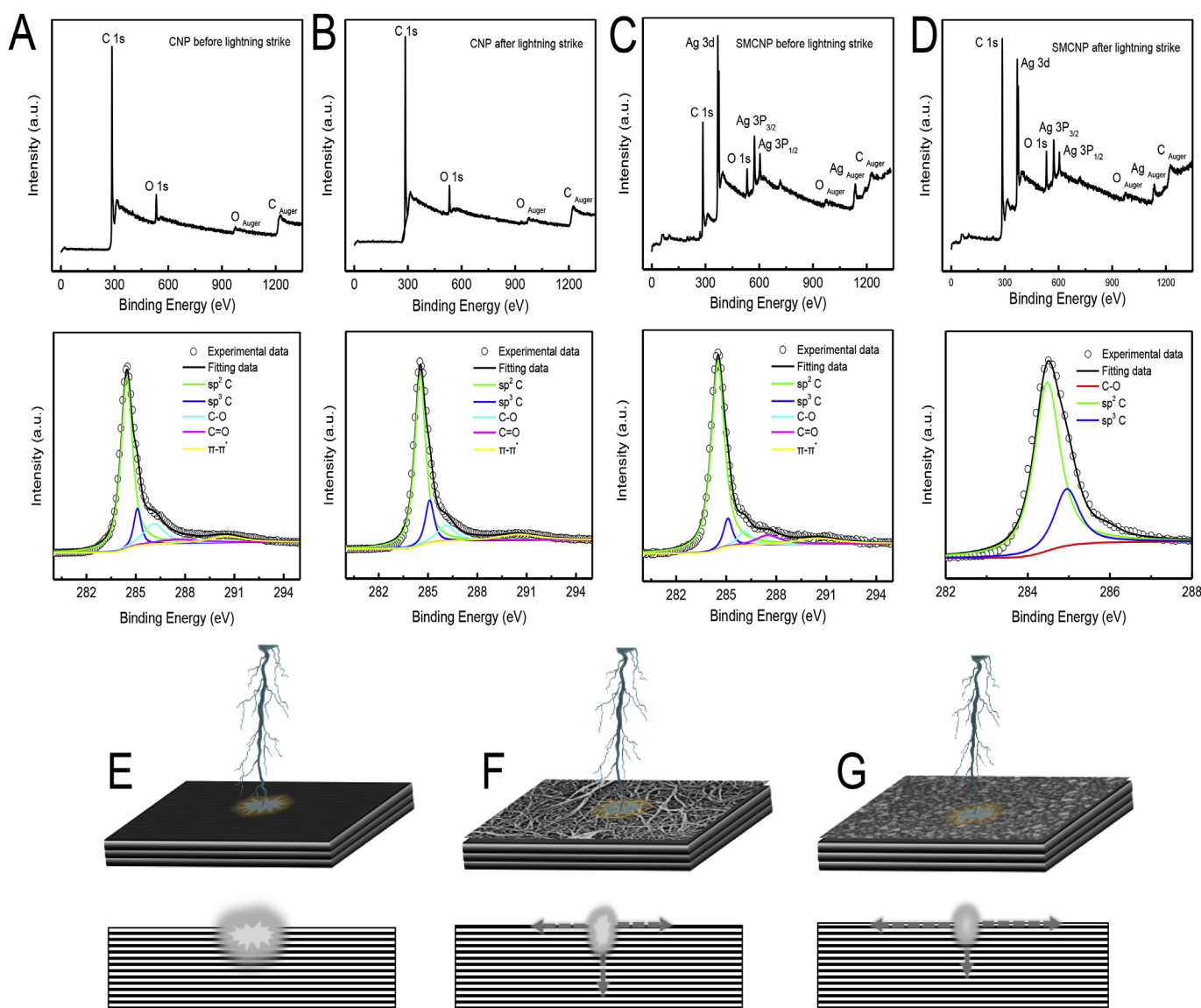
Fig. 7. XPS survey scan and deconvolution of C1s peak of (A) CNP before LS; (B) CNP after LS; (C) SMCNP before the LS; (D) SMCNP after LS. Schematic diagram of the protection mechanism of (E) neat CFRP panel; (F) CNP-CFRP panel; (G) SMCNP-CFRP panel. (A colour version of this figure can be viewed online.)
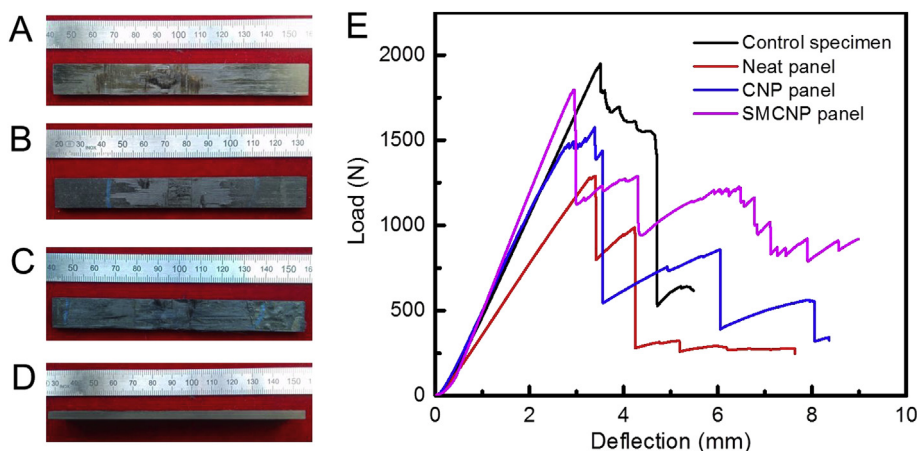
Fig. 8. Three point bending specimens of (A) neat CFRP panel; (B) CNP-CFRP panel; (C) SMCNP-CFRP panel; (D) cross section view. (E) Residual mechanical property of the LS applied specimens of the different panels. (A colour version of this figure can be viewed online.)

XPS analysis results of CNP and SMCNP are listed in Table 1 with the atomic concentration of different chemical carbon atoms. Typically, the atomic concentration of sp^3 C (defects on CNT) of CNP and SMCNP increases by 4.3 and 16.4, respectively, after LS interaction. The rise of defective carbon atom (sp^3 C) indicates partial graphite-like carbon atoms are transformed to defective carbon atoms affected by the high LS energy. In particular, atomic concentration of SMCNP after LS increases by 225% which is much higher than the case of CNP after LS (49%) in agreement with the Raman analysis on the value of I_D/I_G. In addition, the total amount of carbon singly bond to oxygen and carbon doubly bond to oxygen are decreased after LS of CNP and SMCNP, because the combustion reaction transforms the carbon oxygen bond to carbon dioxide or carbon monoxide at the moment of LS.

According to the above analysis, the schematic diagrams of the protection mechanism are shown in Fig. 7(E-G). Due to a bad conductor of the neat panel (Fig. 7E), the lightning current is difficult to disperse rapidly when the LS attaches on the panel surface lead to serious damage. For the CNP-CFRP panel (Fig. 7F), the interaction Joule heat and air pressure could blow away and combust the protection layer very quickly without enough current conduction time to disperse lightning current through the surface CNP layer. Therefore, the current is conducted in panel and out of the panel pointed in the arrow direction. For the SMCNP-CFRP panel (Fig. 7G), the silver particle not only increases the electrical conductivity but also forms a skeleton shown in Fig. 6B to fix the current conduction path for dispersing energy in a longer period. The length of the arrow indicates the current conduction proportion in different direction. Therefore, carbon fiber damaged area of SMCNP-CFRP is larger than CNP-CFRP but lower damaged depth, due to the lightning current proportion in different direction.

3.6. Residual mechanical property analysis

The residual mechanical property of the different CFRP panels was tested by three point bending test according to the ASTM D638. Fig. 8 (A-D) are the three point bending specimens of neat CFRP, CNP-CFRP panel, SMCNP-CFRP panel, and cross section view. It is obvious carbon fiber damaged area of SMCNP-CFRP specimen is larger than CNP-CFRP specimen. Fig. 8E is the curves of load versus deflection of the corresponding specimens. Residual mechanical property is evaluated from the rupture load, due to the same dimension of each specimen. Rupture load for the control sample, the neat CFRP panel, CNP-CFRP panel, and SMCNP-CFRP panel are

1949 N, 1286 N, 1473 N, and 1795 N, respectively. By comparison with control specimen, the residual strength of Neat panel, CNP-CFRP panel, and SMCNP-CFRP panel is 65.9%, 75.6%, and 92.1%, respectively. In engineering applications, the materials could be reused after maintenance, if the residua mechanical property is over 80% of the control specimen. Therefore, SMCNP-CFRP maintains a positive residual mechanical property after the LS test, which the case achieves the purpose of the LS protection.

4. Conclusions

A scalable sesame-cookie like structural SMCNP is prepared successfully by spray-photolytic method. Silver nanoparticles are embedded in the carbon nanotube framework increasing the electrical conductivity from 323 S/cm to 3600 S/cm (11.4 times) in 14.14 wt% mass of silver nanoparticles and atomic ration of 54.6:1 (C: Ag). A dramatic electrical conductivity increase is achieved modified by a small amount of silver nanoparticles. The integral SMCNP not only increases high electric conductivity, but also provides a melted silver skeleton, due to the specific sesame-cookie structure melted by Joule heat. The skeleton fixes a current conduction path for a long period of time to improve carbon fiber lightning protection. The content of sp^3 C in SMCNP (increased by 225%) is much higher than in CNP (Increase by 49%) after LS interaction detected by XPS and Raman spectrum. Sesame-cookie structure SMCNP-CFRP maintains 92.1% mechanical property enhancing the LS protection effect compared with neat panel (65.9%) and CNP-CFRP (75.6%). The residual mechanical property is a positive value for engineering application indicating SMCNP-CFRP is a feasible strategy for CFRP LS protection.

Acknowledgements

Appendix A. Supplementary data

Supplementary data to this article can be found online at https://doi.org/10.1016/j.carbon.2018.11.022.

References

[1] P.E. Deierling, O.I. Zhupanska, Experimental study of high electric current effects in carbon/epoxy composites, Compos. Sci. Technol. 71 (14) (2011)

1659–1664.

[2] M. Gagné, D. Therriault, Lightning strike protection of composites, Prog. Aero. Sci. 64 (2014) 1–16.

[3] A. Larsson, The interaction between a lightning flash and an aircraft in flight, Compt. Rendus Phys. 3 (10) (2002) 1423–1444.

[4] Y. Hirano, S. Katsumata, Y. Iwahori, A. Todoroki, Artificial lightning testing on graphite/epoxy composite laminate, Compos. Appl. Sci. Manuf. 41 (10) (2010) 1461–1470.

[5] G. Gardner, Lightning strike protection for composite structures, High Perform. Compos. 14 (4) (2006) 44.

[6] J. Gou, Y. Tang, F. Liang, Z. Zhao, D. Firsich, J. Fielding, Carbon nanofiber paper for lightning strike protection of composite materials, Compos. B Eng. 41 (2) (2010) 192–198.

[7] P. Feraboli, M. Miller, Damage resistance and tolerance of carbon/epoxy composite coupons subjected to simulated lightning strike, Compos. Appl. Sci. Manuf. 40 (6) (2009) 954–967.

[8] E.M. Bazelyan, Y.P. Raizer, Lightning Physics and Lightning Protection, CRC Press, 2000.

[9] A. Larsson, A. Delannoy, P. Lalande, Voltage drop along a lightning channel during strikes to aircraft, Atmos. Res. 76 (1) (2005) 377–385.

[10] L.M. Gammon, A. Falcone, Lightning strike damage in polymer composites, Adv. Mater. Process. 161 (8) (2003) 61–62.

[11] E. Logakis, A. Skordos, In Lightning strike performance of carbon nanotube loaded aerospace composites, in: 15th European Conference on Composite Materials. Venice, Italy, 2012, pp. 1–6.

[12] G. Gardiner, Lightning strike protection for composite structures, High Perform. Compos. 5 (2006).

[13] A. Fisher, J. Plumer, Lightning Protection of Aircraft, 1977.

[14] R.W. Revie, H.H. Uhlig, Corrosion and Corrosion Control: an Introduction to Corrosion Science and Engineering, fourth ed., Wiley, 2008, p. 98, 98.

[15] D. Brosius, Boeing 787 Update. High Performance Composites, 2007.

[16] T. Ogasawara, Y. Hirano, A. Yoshimura, Coupled thermal–electrical analysis for carbon fiber/epoxy composites exposed to simulated lightning current, Jpn. Soc. Aeronaut. Space Sci. 41 (8) (2010) 973–981.

[17] T.W. Chou, L. Gao, E.T. Thostenson, Z. Zhang, J.H. Byun, An assessment of the science and technology of carbon nanotube-based fibers and composites, Compos. Sci. Technol. 70 (1) (2010) 1–19.

[18] M.H. Al-Saleh, U. Sundararaj, A review of vapor grown carbon nanofiber/polymer conductive composites, Carbon 47 (1) (2009) 2–22.

[19] D.K. Chakravarthi, V.N. Khabashesku, R. Vaidyanathan, J. Blaine, S. Yarlagadda, D. Roseman, et al., Carbon fiber-bismaleimide composites filled with nickel-coated single-walled carbon nanotubes for lightning-strike protection, Adv. Funct. Mater. 21 (13) (2011) 2527–2533.

[20] F.A. Fischer, Lightning Protection of Aircraft, Lightning Technologies Inc., 2014.

[21] C. Karch, et al., Lightning protection of carbon fibre reinforced plastics - an overview, in: 33rd International Conference on Lightning Protection (ICLP), 2016.

[22] J.J. Zheng, X. Tong, A review on polymer/carbon nanotube composites, Plastics 35 (6) (2006) 65–70.

[23] J.E. Yagoubi, G. Lubineau, S. Saghir, J. Verdu, A. Askari, Thermomechanical and hygroelastic properties of an epoxy system under humid and cold-warm cycling conditions, Polym. Degrad. Stabil. 99 (2014) 146–155.

[24] J.E. Yagoubi, G. Lubineau, F. Roger, J. Verdu, A fully coupled diffusion-reaction scheme for moisture sorptiondesorption in an anhydride-cured epoxy resin, Polymer 53 (2012) 5582–5595.

[25] Y. Tonozuka, I. Shohji, S. Koyama, H. Hokazono, Degradation behaviors of adhesion strength between epoxy resin and copper under aging at high temperature, Procedia Engineering 184 (2017) 648–654.

[26] M. Lafarie-Frenot, S. Rouquié, N. Ho, V. Bellenger, Comparison of damage development in c/epoxy laminates during isothermal ageing or thermal cycling, Composites Part A 37 (2006) 662–671.

[27] R. Krishnamoorti, Strategies for dispersing nanoparticles in polymers, MRS Bull. 32 (4) (2007) 341–347.

[28] J. Baur, E. Silverman, Challenges and opportunities in multifunctional nanocomposite structures for aerospace applications, MRS Bull. 32 (4) (2007) 328–334.

[29] B. Zhang, V.R. Patlolla, D. Chiao, D.K. Kalla, H. Misak, R. Asmatulu, Galvanic corrosion of Al/Cu meshes with carbon fibers and graphene and ITO-based nanocomposite coatings as alternative approaches for lightning strikes, Int. J. Adv. Manuf. Technol. 67 (5–8) (2013) 1317–1323.

[30] J.H. Han, H. Zhang, M.J. Chen, D. Wang, Q. Liu, Q.L. Wu, et al., The combination of carbon nanotube buckypaper and insulating adhesive for lightning strike protection of the carbon fiber/epoxy laminates, Carbon 94 (2015) 101–113.

[31] I.W. Chen, R. Liang, H. Zhao, B. Wang, C. Zhang, Highly conductive carbon nanotube buckypapers with improved doping stability via conjugational cross-linking, Nanotechnology 22 (48) (2011) 3392–3398.

[32] Z. Wang, Z. Liang, B. Wang, C. Zhang, L. Kramer, Processing and property investigation of single-walled carbon nanotube (SWNT) buckypaper/epoxy resin matrix nanocomposites, Composites Part A Applied Science & Manufacturing 35 (10) (2004) 1225–1232.

[33] R.H. Baughman, C. Cui, A.A. Zakhidov, Z. Iqbal, J.N. Barisci, G.M. Spinks, et al., Carbon nanotube Actuators, Science 284 (5418) (1999) 1340–1344.

[34] M. Wenjun, L. Song, R. Yang, Z. Taihua, Z. Yuanchun, S. Lianfeng, et al., Directly synthesized strong, highly conducting, transparent single-walled carbon nanotube films, Nano Lett. 7 (8) (2007) 2307–2311.

[35] J. Zhang, D. Jiang, H.X. Peng, F. Qin, Enhanced mechanical and electrical properties of carbon nanotube buckypaper by in situ cross-linking, Carbon 63 (63) (2013) 125–132.

[36] D. Wang, P. Song, C. Liu, W. Wu, S. Fan, Highly oriented carbon nanotube papers made of aligned carbon nanotubes, Nanotechnology 19 (7) (2008) 369–381.

[37] J.W. Han, J. Kim, J. Li, M. Meyyappan, Carbon nanotube based humidity sensor on cellulose paper, J. Phys. Chem. C 116 (41) (2012) 22094–22097.

[38] D. Antiohos, G. Folkes, P. Sherrell, S. Ashraf, G.G. Wallace, P. Aitchison, et al., Compositional effects of PEDOT-PSS/single walled carbon nanotube films on supercapacitor device performance, J. Mater. Chem. 21 (40) (2011) 15987–15994.

[39] H. Chu, Z. Zhang, Y. Liu, J. Leng, Self-heating fiber reinforced polymer composite using meso/macropore carbon nanotube paper and its application in deicing, Carbon 66 (1) (2014) 154–163.

[40] Z. Tang, C.H. Tang, H. Gong, A high energy density asymmetric supercapacitor from nano-architectured Ni(OH)2/Carbon nanotube electrodes, Adv. Funct. Mater. 22 (6) (2012) 1272–1278.

[41] H. Chu, Z. Zhang, Y. Liu, J. Leng, Silver particles modified carbon nanotube paper/glassfiber reinforced polymer composite material for high temperature infrared stealth camouflage, Carbon 98 (2016) 557–566.

[42] B. Fugetsu, E. Sano, M. Sunada, Y. Sambongi, T. Shibuya, X. Wang, et al., Electrical conductivity and electromagnetic interference shielding efficiency of carbon nanotube/cellulose composite paper, Carbon 46 (9) (2008) 1256–1258.

[43] G. Labate, L. Matekovits, Kirchhoff's Current Law as Local Cloaking Condition: Theory and Applications, 2016.

[44] A. Patole, G. Lubineau, Carbon nanotubes with silver nanoparticle decoration and conductive polymer coating for improving the electrical conductivity of polycarbonate nanocomposites, Carbon 81 (2015) 720–730.

[45] A. Patole, I.A. Ventura, G. Lubineau, Thermal conductivity and stability of a three-phase blend of carbon nanotubes, conductive polymer, and silver nanoparticles incorporated into polycarbonate nanocomposites, J. Appl. Polym. Sci. 132 (30) (2015) 42281.

[46] M.M. Zaeri, S. Ziaei-Rad, A. Vahedi, F. Karimzadeh, Mechanical modelling of carbon nanomaterials from nanotubes to buckypaper, Carbon 48 (13) (2010) 3916–3930.

[47] B. Lepetit, C. Escure, S. Guinard, I. Revel, G. Peres, Thermo-mechanical effects induced by lightning on carbon fiber composite materials, in: International Conference on Lightning and Static Electricity, ICOLSE, Oxford, 2011.

[48] C. Karch, W. Wulbrand, Thermomechanical Damage of Protected CFRP Structures Caused by Lightning Continuous Currents, SEA2013-20.1, ICOLSE, 2013.

[49] C. Karch, A. Arteiro, F. Nobis, Y. Duval, J. Wolfrum, Modelling and Simulation of Lightning-induced Damage of CFRP Structures, ICOLSE, 2017.

[50] Q. Dong, Y. Guo, J. Chen, X. Yao, X. Yi, L. Ping, Y. Jia, Influencing factor analysis based on electrical–thermal-pyrolytic simulation of carbon fiber composites lightning damage, Compos. Struct. 140 (2016) 1–10.